

## PHYSICS CONTRIBUTION

# QUANTITATIVE ULTRASOUND CHARACTERIZATION OF CANCER RADIOTHERAPY EFFECTS *IN VITRO*

ROXANA M. VLAD, M.Sc.,\*<sup>†</sup> NEHAD M. ALAJEZ, Ph.D.,\* ANOJA GILES, B.Sc.,<sup>†</sup>  
MICHAEL C. KOLIOS, Ph.D.,\*<sup>‡</sup> AND GREGORY J. CZARNOTA, Ph.D., M.D.\*<sup>†§</sup>

Departments of \*Medical Biophysics and <sup>§</sup>Radiation Oncology, University of Toronto, Toronto, ON, Canada; <sup>†</sup>Sunnybrook Health Sciences Centre, Toronto, ON, Canada; and <sup>‡</sup>Department of Physics, Ryerson University, Toronto, ON, Canada

**Purpose:** Currently, no routinely used imaging modality is available to assess tumor responses to cancer treatment within hours to days after radiotherapy. In this study, we demonstrate the preclinical application of quantitative ultrasound methods to characterize the cellular responses to cancer radiotherapy *in vitro*.

**Methods and Materials:** Three different cell lines were exposed to radiation doses of 2–8 Gy. Data were collected with an ultrasound scanner using frequencies of 10–30 MHz. As indicators of response, ultrasound integrated backscatter and spectral slope were determined from the cell samples. These parameters were corrected for ultrasonic attenuation by measuring the attenuation coefficient.

**Results:** A significant increase in the ultrasound integrated backscatter of 4–7 dB ( $p < 0.001$ ) was found for radiation-treated cells compared with viable cells at all radiation doses. The spectral slopes decreased in the cell samples that predominantly underwent mitotic arrest/catastrophe after radiotherapy, consistent with an increase in cell size. In contrast, the spectral slopes did not change significantly in the cell samples that underwent a mix of cell death (apoptosis and mitotic arrest), with no significant change in average cell size.

**Conclusion:** The changes in ultrasound integrated backscatter and spectral slope were direct consequences of cell and nuclear morphologic changes associated with cell death. The results indicate that this combination of quantitative ultrasonic parameters has the potential to assess the cell responses to radiation, differentiate between different types of cell death, and provide a preclinical framework to monitor tumor responses *in vivo*. Crown Copyright © 2008 Published by Elsevier Inc.

Ultrasound backscatter, Spectral slope, Radiotherapy, Apoptosis, Mitotic arrest/catastrophe.

## INTRODUCTION

In clinical oncology and experimental therapeutics, changes in tumor growth rate or volume have been traditionally used as a first indication of the treatment response. These changes typically occur late in the course of therapy. Currently, no routinely used clinical imaging modality is available to assess tumor responses to cancer treatment within hours to days after radiotherapy. Computed tomography (CT) and positron emission tomography (PET) imaging or combined CT/PET imaging have been used to assess tumor responses to cancer therapies, typically 3–4 weeks after treatment initiation (1, 2). Dynamic contrast-enhanced magnetic resonance imaging measurements have been observed to correlate with immunohistochemical

measures of tumor anti-angiogenesis (3, 4) within the same timeframe. Dynamic contrast-enhanced Doppler ultrasonography has been successful in predicting the early tumor response in isolated limb perfusion of limb sarcomas (5) within 1–7 days after therapy delivery. However, the use of such imaging modalities to monitor the response of tumors to cancer therapies can be limited by either their cost (dynamic contrast-enhanced magnetic resonance imaging, PET, CT, combined PET/CT) or limited applicability (dynamic contrast-enhanced Doppler ultrasonography). The ability to assess early tumor responsiveness to therapy within days after the start of treatment could ultimately aid clinicians in making decisions to modify therapy (*e.g.*, choosing different radiation regimens, adding

Reprint requests to: Gregory J. Czarnota, Ph.D., M.D., Department of Radiation Oncology, Sunnybrook Health Sciences Centre, 2075 Bayview Ave., Toronto, ON M4N 3M5 Canada. Tel: (416) 480-5329; Fax: (416) 480-6002; E-mail: [Gregory.Czarnota@sunnybrook.ca](mailto:Gregory.Czarnota@sunnybrook.ca)

Supported by American Institute of Ultrasound in Medicine's Endowment for Education and Research Grant, Canadian Institutes of Health Research Strategic Training Fellowship Excellence in Radiation Research for the 21st Century, Canadian Foundation of Innovation/Ontario Innovation Trust, Ryerson University, Sunnybrook

Health Sciences Centre, and Natural Sciences Engineering Research Council of Canada Cancer Care Ontario Cancer Imaging Network of Ontario grants.

Conflict of interest: none.

**Acknowledgments**—We gratefully thank Drs. Peter Burns and Fei-Fei Liu for valuable discussion and Drs. Deborah Foster and Fei-Fei Liu for providing some of the cell lines used in this study.

Received April 14, 2008, and in revised form June 24, 2008. Accepted for publication July 9, 2008.

a radiosensitizer, or using different chemotherapy drugs that potentially could result in more effective treatment, leading to improved outcomes and sparing patients unnecessary side effects).

The ultrasonic scattering process in biologic tissues is primarily affected by the size, acoustic impedance ( $Z = \sqrt{\rho/\kappa}$ , where  $\rho$  is the density and  $\kappa$  is the compressibility), and the spatial distribution of tissue-scattering structures. Ultrasonic tissue characterization techniques are based on the premise that disease processes or therapies alter the physical characteristics of tissue (*i.e.*, compressibility, density, and scatterer size), and these alterations cause observable changes in acoustic scattering properties. The characterization of tissue microstructures by examining the frequency-dependent backscatter has been used to diagnose prostate cancer, ocular tumors, and cardiac and liver abnormalities (6–8) and to differentiate benign fibroadenomas from mammary carcinomas and sarcomas (9). It has also provided good diagnostic accuracy in the detection and lesion localization of prostate cancer (10, 11).

The aim of cancer radiotherapy is to kill tumors by inducing cell death, including apoptosis or mitotic arrest/catastrophe (12). Currently, the standard methods for detecting cell death are invasive and involve special staining. Previous studies have indicated that high-frequency ultrasound (*i.e.*, 10–60 MHz) is sensitive to apoptosis *in vitro* and *in vivo* (13). In previous studies, the backscatter intensity from apoptotic cells has exhibited an  $\leq 16$ -fold increase compared with viable cells (13, 14). In addition, the spectral slope was observed to increase significantly for apoptotic cells vs. viable cells (14). For the range of ultrasonic frequencies used in these studies of 10–60 MHz, the corresponding ultrasound wavelengths of 25–150  $\mu\text{m}$  approach the size of cells and nuclei (10–20  $\mu\text{m}$ ) and, hence, are more sensitive to changes in cellular and nuclear structure than conventional ultrasound (15).

In this study, we investigated whether ultrasound imaging, ultrasound integrated backscatter (UIB), and spectral slope (SS), calculated from ultrasound power spectra, can be used in the laboratory to monitor the responses of tumor cells exposed to radiotherapy. This study represents the first evidence of the use of spectral parameters to detect radiotherapy effects *in vitro*, specifically differentiating between cells that die predominantly by mitotic arrest/catastrophe from cells that die predominantly by a mix of apoptosis and mitotic arrest.

Three different cell lines were used in this study: AML, FaDu, and Hep-2. The AML cell line was used as a reference model because the apoptotic response of this cell line to a chemotherapeutic drug has been histologically and ultrasonically well-characterized previously (13, 14). The head-and-neck cancer cell lines (FaDu and Hep-2) were chosen because a primary treatment modality for head-and-neck cancers is radiotherapy.

## METHODS AND MATERIALS

### Cell preparation

Acute myeloid leukemia cells (OCI-AML-5) (16) were grown from frozen stock samples as described previously (17). The human head-and-neck tumor cell lines, FaDu and Hep-2, were obtained from the American Type Culture Collection (Manassas, VA).

Hep-2 was cultured in  $\alpha$ -minimum essential media supplemented with 0.1% gentamicin and 10% fetal bovine serum. FaDu was cultured in Eagle's minimum essential medium with 2 mM L-glutamine and Earle's balanced salt solution adjusted to contain 1.5 g/L sodium bicarbonate, 1.0 mM sodium pyruvate, and 10% fetal bovine serum. All cell lines were grown in a humidified atmosphere at 37°C, containing 5% carbon dioxide.

The cell samples were irradiated using a small animal and cell irradiator (Faxitron Cabinet X-ray System, Faxitron X-ray, Wheeling, IL). This delivered 160-keV X-rays at a rate of 200 cGy/min for doses of 2, 4, and 8 Gy. The structural changes that are characteristic of apoptotic and mitotic response (*i.e.*, increase in cell and nuclei size, membrane ruffling, cytoplasm vacuolization, nuclei fragmentation and condensation, and formation of apoptotic and mitotic bodies) were used as an indication of responses to radiotherapy. These structural changes were observed in the AML cell culture for all applied radiation doses and at 8 Gy for the FaDu and Hep-2 cell lines at 48 h after exposure to radiotherapy. The cell samples were ultrasonically imaged 48 h after exposure to radiotherapy because keeping the treated cells >2 days in the culture would allow the surviving cells to further divide, decreasing the chance to effectively image the early radiation effects. The 8-Gy radiation dose is consistent with the large palliative doses administered in the clinic to obtain appreciable rapid clinical effects.

Before ultrasound data acquisition, the cells were trypsinized (Hep-2 and FaDu), washed in phosphate-buffered saline, and centrifuged at 1900g. Parallel samples consisting of untreated (control) and treated cells were prepared by centrifugation in a custom-built sample holder. The sample holder had three cylindrical holes of 8 mm  $\times$  7 mm (diameter  $\times$  height). The treated and control samples were prepared by centrifugation of cells in two separate wells. The other well, containing phosphate-buffered saline, served as a calibration reference. The cell samples were independently prepared in triplicate from different sets of cells.

### Ultrasound data acquisition and analysis

A VS40B high-frequency ultrasound device (VisualSonics, Toronto, ON, Canada) was used to image cell samples. A transducer with a nominal center frequency of 20 MHz and a  $-6$ -dB bandwidth of 12–30 MHz was used to collect the ultrasound data. The data were collected within the transducer depth of field (3.12 mm) from five different planes containing 40–60 scan lines each and stored digitally at a sampling rate of 500 MHz. Five regions of interest (ROIs) containing 15–25 independent scan lines separated by a distance of 250  $\mu\text{m}$  (the transducer beam width at the nominal center frequency) were chosen to calculate the backscattered power spectra. These ROIs were 1 mm in height, centered around the transducer focus.

Ultrasound scan lines from each bracketed line segment were multiplied by a Hamming weighting function to suppress the spectral lobes, and the Fourier transform was computed. The squared magnitudes of the resultant spectra from all ROIs were averaged and divided by the power spectrum computed from a flat quartz calibration target to calculate the normalized power spectra. This procedure removed system and transducer transfer functions to provide a common reference for data collected using various transducers and systems (18). The normalized power spectra were compensated for frequency-dependent attenuation according to Taggart *et al.* (17). The resulting normalized power spectra were integrated over the transducer  $-6$ -dB bandwidth to calculate the UIB. Linear regression analysis was used to calculate the SS from the normalized backscatter power. The SS is a putative indicator of effective scatterer size, and a decrease in SS corresponds with an increase in effective scatterer

Table 1. ATS, SOS, UIB, average diameter  $\pm$  variance, and SS measured for all cell samples

Cell type	ATS $\pm$ SE (dB/mm/MHz)	SOS $\pm$ SE (m/s)	UIB $\pm$ SE (dB)	Cell size ( $\mu\text{m}$ ) $\pm$ variance ( $\mu\text{m}^2$ )	SS $\pm$ SE (dB/MHz)
AML control	0.054 $\pm$ 0.002	1,530 $\pm$ 2	-55.4 $\pm$ 0.3	10.3 $\pm$ 2.3	0.89 $\pm$ 0.08
AML 2 Gy	0.063 $\pm$ 0.005	1,501 $\pm$ 6	-51.6 $\pm$ 0.6	10.4 $\pm$ 4.5	0.91 $\pm$ 0.05
AML 4 Gy	0.060 $\pm$ 0.007	1,516 $\pm$ 5	-48.3 $\pm$ 0.5	9.2 $\pm$ 5.2	0.84 $\pm$ 0.06
AML 8 Gy	0.055 $\pm$ 0.008	1,514 $\pm$ 3	-49.6 $\pm$ 0.6	9.9 $\pm$ 4.6	0.85 $\pm$ 0.10
FaDu control	0.070 $\pm$ 0.002	1,532 $\pm$ 4	-50.5 $\pm$ 0.7	16.6 $\pm$ 7.5	0.53 $\pm$ 0.07
FaDu 8 Gy	0.068 $\pm$ 0.003	1,499 $\pm$ 2	-46.3 $\pm$ 0.8	19.9 $\pm$ 19.1	0.34 $\pm$ 0.08
Hep-2 control	0.060 $\pm$ 0.007	1,540 $\pm$ 7	-52.3 $\pm$ 0.4	17.4 $\pm$ 5.4	0.57 $\pm$ 0.04
Hep-2 8 Gy	0.059 $\pm$ 0.005	1,543 $\pm$ 3	-45.9 $\pm$ 0.6	18.0 $\pm$ 14.1	0.44 $\pm$ 0.07

*Abbreviations:* ATS = attenuation coefficient slope; SOS = speed of sound; UIB = ultrasound integrated backscatter; SS = spectral slope; SE standard error of average ultrasound parameters.

Three cell samples were considered for each experimental condition.

size when properly corrected for attenuation, according to Lizzi *et al.* (6). Additional details on the theoretical and signal analysis considerations can be found in publications by Lizzi *et al.* (7, 19).

The speed of sound (SOS) and attenuation coefficient slope (ATS) were obtained by repeating each of the measurements on three different ROIs on the same cell sample. A time-of-flight method (20) was used to calculate the SOS. The thickness of the cell sample was calculated as  $D = \text{SOS} \times t/2$ , where  $t$  is the difference in the mean times of arrival of reflections from the bottom of the well containing the cell sample and the top of the cell sample. The thickness of the cell sample was used to calculate the ATS as a function of frequency using a broadband technique (20). A detailed presentation of data collection and analysis of ATS and SOS are described in a recent publication (17).

### Statistical analysis

Statistical analysis was performed using GraphPad Prism (GraphPad Software, San Diego, CA). A  $t$  test was applied to each combination of conditions, and  $p < 0.05$  was considered significant. The ultrasonic parameters calculated from all ultrasound scan lines for one treatment condition, considered as one population, were compared against the ultrasonic parameters computed from the corresponding control sample for the FaDu and Hep-2 cell lines. One-way analysis of variance was applied to test the changes in the ultrasonic parameters calculated from all three treatment conditions considered for the AML cell line. The Bonferroni correction was applied to the probability value, and  $p < 0.0167$  was considered significant.

### Cytology analysis, cell size, and morphology measurements

To investigate the morphology of cells at each experimental condition, ultrasonically imaged samples were fixed for 24 h in 10% buffered formalin, embedded in paraffin, and processed as histologic sections. Hematoxylin and eosin staining and phase contrast microscopy images were used to assess the general cell morphology. The cell and nuclear fragment sizes for each experimental condition were measured with a Multisizer3 Coulter Counter (Beckman Coulter, Mississauga, ON, Canada) using a 100- $\mu\text{m}$  aperture that allowed for precise and reliable particle size measurements in the 5–60- $\mu\text{m}$  range. Flow cytometric analysis using propidium iodine was performed to measure cell DNA content using a FACS caliber (BD Biosciences, Mississauga, ON, Canada), as described previously (21).

## RESULTS

The values of ATS, SOS, UIB, cell size, and SS for all viable and treated cell samples are presented in Table 1. No statistically significant differences were observed between the ATS and SOS values calculated for each cell line from the viable and irradiated cell samples.

The UIB increased for all three cell lines (FaDu, Hep-2, and AML) exposed to radiotherapy, by 3.8–7.1 dB ( $p < 0.001$ ; Table 1). Figure 1 shows two representative ultrasound images of an untreated and treated Hep-2 cell sample corresponding to the UIB values presented in Table 1.

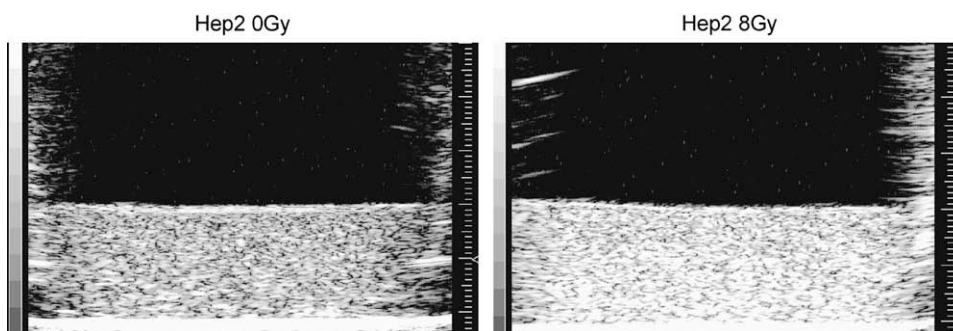


Fig. 1. Representative ultrasound images of Hep-2 cell samples demonstrating increase in ultrasound backscatter, observed as increase in image brightness (approximately fourfold increase) after radiation. Height of cell sample is  $\sim 2$  mm. Smallest division on scale on lateral side of each pellet is 0.1 mm. Small triangle on right side of each cell sample represents location of transducer focal point. The hyperechoic line across bottom of ultrasound image is bottom of sample holder.

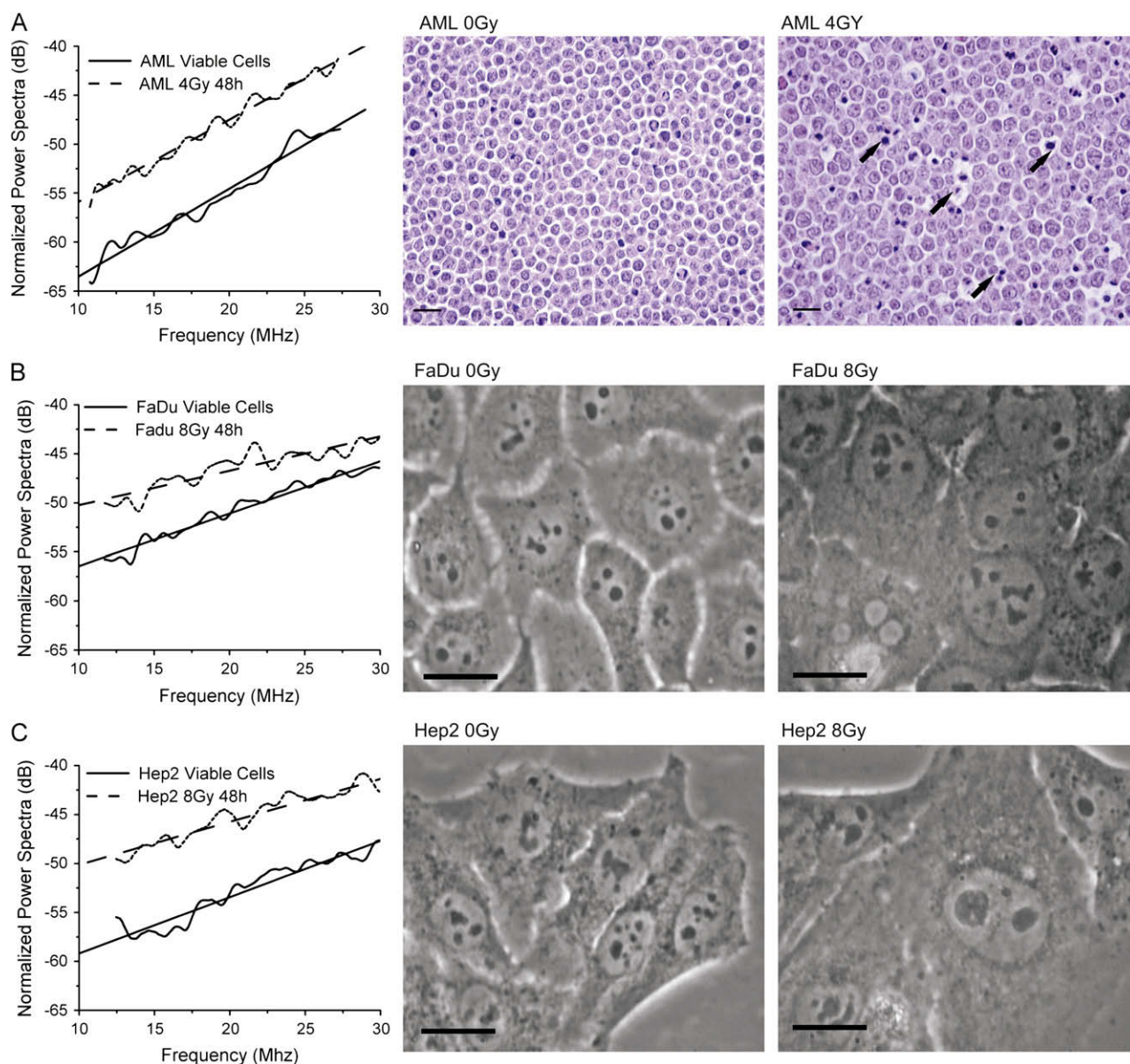


Fig. 2. Normalized power spectra and microscopy images before and after treatment for (A) AML, (B) FaDu, and (C) Hep-2 cell samples. Scale bars in hematoxylin and eosin and phase microscopy slides represent 20  $\mu\text{m}$ .

Spectral slope can be related to the size of the major scattering structures in a sample (6, 22). In the present study, the SS revealed different trends, depending on the changes in the cell/nuclear sizes after different modalities of cell death. The SS calculated for the AML cell samples did not change significantly between the viable and treated samples or between the samples treated with different radiation doses (Table 1 and Fig. 2A). The corresponding hematoxylin and eosin image of the AML cells treated with radiotherapy exhibited a mix of cell death: apoptosis with nuclear condensation and fragmentation, and mitotic arrest with enlarged cells (Fig. 2A). The SS calculated for the Hep-2 and FaDu cell samples decreased with radiation by 20–40% ( $p < 0.05$ ; Table 1 and Fig. 2B). Phase contrast microscopy images of the two head-and-neck cancer cell lines, FaDu and Hep-2, exhibited the morphologic characteristics of only

mitotic arrest/catastrophe with enlarged cells and nuclei after exposure to 8 Gy radiation (Figs. 2B,C). The decrease in the SS can be interpreted as an increase in the average scatterer size, consistent with the observed increase in cell/nuclear sizes.

To identify the modalities of cell death after radiotherapy, in addition to histologic examination, flow-cytometric measurements of DNA content were performed. Because the nucleus becomes fragmented during apoptosis, sub- $G_1$  fractions were identified as apoptotic cells. The sub- $G_1$  peak can represent, in addition to apoptotic cells, mechanically damaged cells and cell fragments resulting from advanced stages of cell death (21, 23). The  $G_2/M$  peak was identified as cells in mitosis and mitotic arrest, and the peak with greater than double DNA content (greater than in the  $G_2/M$  fraction) was identified as cells in mitotic catastrophe and polyploid

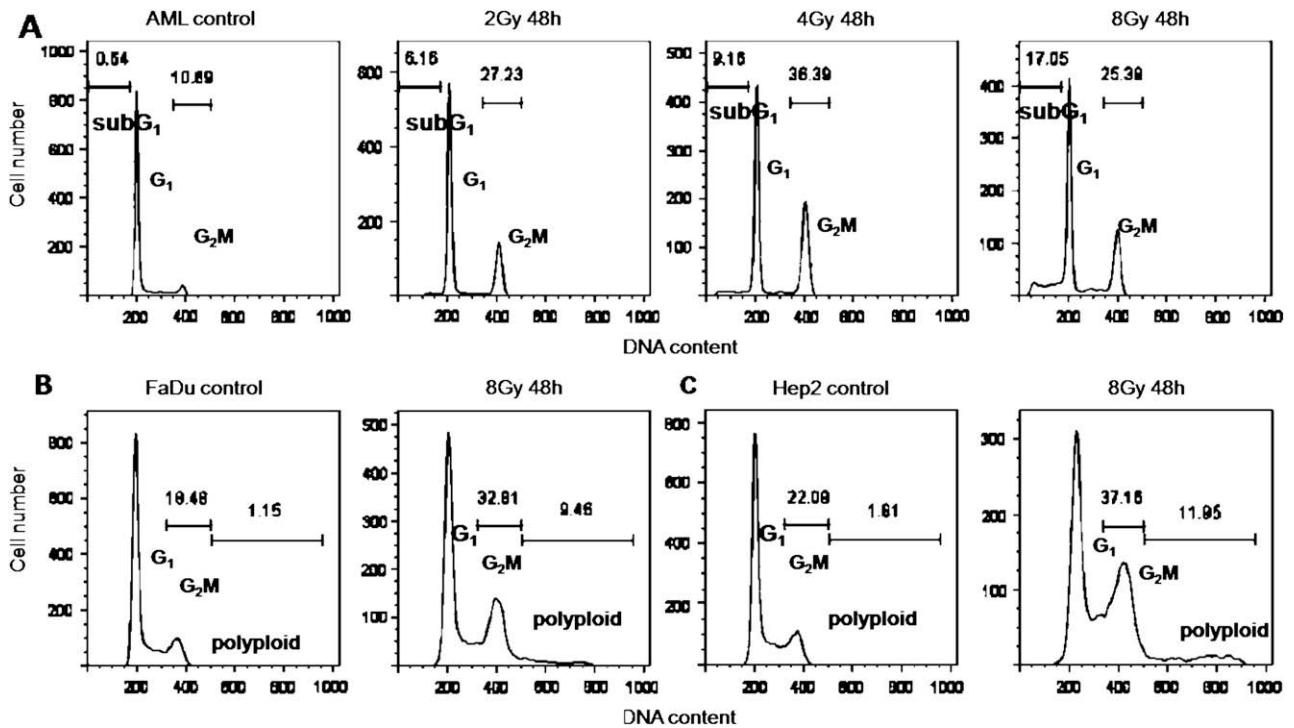


Fig. 3. Flow-cytometric measurement of cellular DNA content. (A) AML cell samples demonstrating increase in apoptotic and mitotic cell fractions illustrated by sub-G<sub>1</sub> fraction (0.64%, 0 Gy; 6.16%, 2 Gy; 9.16%, 4 Gy; 17.05%, 8 Gy) and G<sub>2</sub>/M fraction (10.69%, 0 Gy; 27.23%, 2 Gy; 36.39%, 4 Gy; 25.39%, 8 Gy). (B) FaDu and (C) Hep-2 demonstrating increase in G<sub>2</sub>/M fraction (FaDu: 18.48%, 0 Gy and 32.81%, 8 Gy; Hep-2: 22.09%, 0 Gy and 37.16%, 8 Gy) and polyploid fraction (FaDu: 1.15%, 0 Gy and 9.46%, 8 Gy; Hep-2: 1.61%, 0 Gy and 11.95%, 8 Gy) after radiotherapy, consistent with mitotic arrest/catastrophe.

cells. Cells typically die by mitotic arrest/catastrophe after they undergo up to four unsuccessful mitotic cycles, as described by Tannock *et al.* (12). The analysis of the DNA content for the AML cell samples demonstrated a mix of cell death by apoptosis, with a 25-fold maximal increase in the sub-G<sub>1</sub> fraction and a 3.5-fold maximal increase in the G<sub>2</sub>/M cell fraction (Fig. 3A). For the head-and-neck cancer cell lines, no sub-G<sub>1</sub> fractions were detectable, but an approximately twofold increase in the mitotic cell fraction (G<sub>2</sub>/M) and a six- to eightfold increase in the mitotic catastrophe and polyploid cell fraction (Fig. 3B,C) was found.

Scatterer size can be a major determinant of the ultrasound backscatter strength, (indicated in this study by UIB) and of the ultrasound backscatter frequency dependence (indicated in this study by SS). Measurements of cell size distributions were performed to determine how the sequence of cell death affected the cell sizes and to correlate these changes to the ultrasound parameters. Measurement of the cell sizes demonstrated no significant changes in the average AML cell size with treatment (Table 1); however, the cell size distributions changed with exposure to different radiation doses. The cell size distributions revealed an increase in the count of smaller

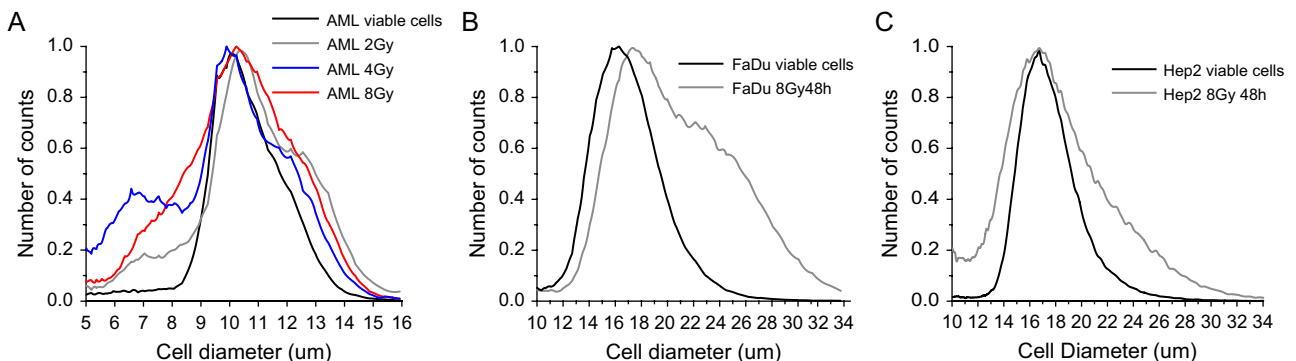


Fig. 4. Histograms of cell size distributions for (A) AML, (B) FaDu, and (C) Hep-2 before and after radiotherapy, demonstrating changes in cell size distributions depending on cell type and radiation dose. Histograms normalized to one by dividing each count from distribution to maximal count.

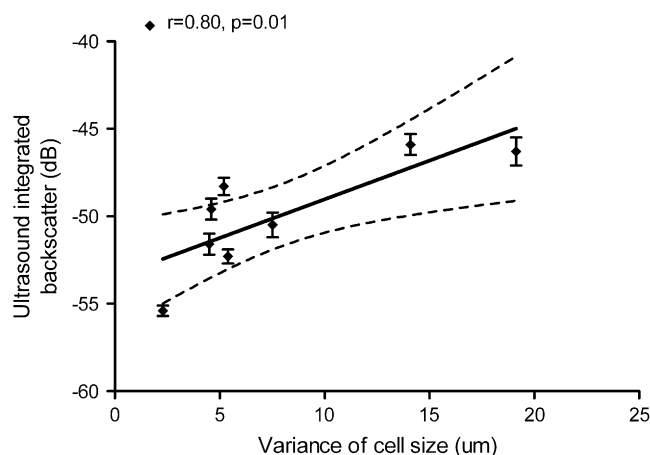


Fig. 5. Linear correlation between ultrasound integrated backscatter and variance of cell sizes measured from all cell samples, viable and exposed to radiotherapy. Curved lines indicate 95% confidence bands of regression line representing boundaries of all possible straight lines, including 95% interval of slopes and intercepts.

particles, consistent with apoptotic cells and nuclear fragments, and an increase in the count of larger particles, consistent with mitotically arrested cells (Fig. 4). An increase in the count of particles with larger sizes was measured for FaDu and Hep-2 cells, consistent with the cell death by mitotic arrest/catastrophe exhibited by these cell lines (Fig. 4B,C).

In the present study, we also investigated the variance of cell sizes (the squared standard deviation), because it can considerably influence cell and nuclei spatial organization in a sample (24, 25). The UIB measured from all cell samples correlated well with the variance of cell sizes, with a Pearson correlation coefficient of  $r = 0.80$  and statistical significance of  $p < 0.01$  (Fig. 5). The goodness of fit of the linear regression was  $r^2 = 0.64$ , suggesting that the increase in cell size variance might have a contribution to the increase in ultrasound backscatter.

## DISCUSSION

The present study has demonstrated the use of ultrasonic spectral parameters to detect cell responses to radiotherapy and to differentiate the cells that die predominantly by mitotic arrest/catastrophe from the cells that die predominantly by a mix of apoptosis and mitotic arrest. The changes in ultrasonic parameters were direct consequences of cell structural changes following the sequence of cell death and, hence, provide a basis for characterizing tumor responses to radiotherapy in preclinical mouse cancer models (26). The SOS and ATS were used to correct the normalized power spectra for frequency-dependent attenuation and provided an understanding of how attenuation and SOS can change with radiotherapy. This constitutes essential information for the application of this technique *in vivo* in mouse cancer tumors grown from the same type of tumor cell lines (26).

Ultrasonic parameters, including SS and UIB, have previously been used to characterize diseased tissue or tissue and

cell samples exposed to different therapeutic agents (6, 8, 10, 14, 17, 27). In the present study, the UIB increased in all cell samples exposed to radiotherapy. The UIB depends on the size, acoustic properties (density and compressibility), and spatial arrangement of scatterers in a sample. Previous studies have demonstrated an increase in ultrasound backscatter *in vitro* and *in vivo* for cell samples exposed to chemotherapeutic drugs, photodynamic therapy (13, 14), and ischemic injury (27). The mechanism behind this increase was broadly linked to the cell and nuclear morphologic changes observed histologically during cell death. The present study has confirmed these observations using three cell lines exposed to radiotherapy that underwent different types of cell death. Qualitative analysis of cell microscopy images, measurements of cellular DNA content, and measurements of cell size distributions demonstrated that, as expected, the nuclear sizes decreased during cell death by apoptosis and increased during mitotic arrest/catastrophe, followed by similar changes in the cell sizes (Figs. 2–4). The changes in the cell and nuclear sizes during the sequence of cell death resulted in an increase in the variance of cell sizes by more than twofold (Table 1). The increase in the variance in cell sizes might have contributed to the UIB increase, as suggested by the correlation between the UIB and the variance in cell sizes (Fig. 5). Work in progress in our laboratory (28) has indicated a good agreement between the changes measured in the UIB with increasing variance in cell sizes and the simulations of ultrasound scattering with increasing randomization. Other contributions to the UIB increase can be attributed to the changes in size and acoustic impedance of the cells and nuclei during the sequence of cell death. For example, all cell lines exhibited an increase in the count of cells with larger sizes. This was more pronounced for the FaDu cell line (Fig. 4). As another example, the nuclear condensation present in the AML cell line treated with radiotherapy might result in changes in acoustic impedance.

The SS can be used putatively to characterize the size of the major scattering structure in tissue, as demonstrated previously (7, 10, 22, 29, 30). Previous work by Kolios *et al.* (14) demonstrated that the SS increased in the cell samples that predominantly presented classic features of apoptosis, including cell shrinkage and nuclear condensation and fragmentation. In contrast, in the present study, the SS decreased in cell samples that predominantly underwent mitotic arrest/catastrophe and did not change in the cell samples that underwent a mix of apoptosis and mitotic arrest. We have indicated that this detection is determined by the changes in cell and nuclear sizes during different modalities of cell death. Therefore, the SS can be used as an aid to differentiate the predominant form of cell death in cell samples exposed to different types of therapies.

### Implications

The head-and-neck cancer models were chosen in this study because a primary treatment modality for these types of cancers is radiotherapy. Considering future applications of the technique described in the present study, this type of

tumor could be accessed in humans with endoscopic probes working at 10–20 MHz (31). Ultrasound imaging enhanced by ultrasonic spectral parameters could provide the benefit of determining the tumor response early, within days after treatment starts, allowing tumor imaging before and multiple times during treatment. An early indicator of treatment response would be of great value to tailor treatments to individual patients and is particularly promising for multistage interventions or combination treatments.

### Limitations

A penetration depth of 2–5 cm for 10–30-MHz ultrasound allows the technique to be applicable to a variety of tumor types such as skin cancers, certain cancers of the breast, and cancers that can be reached with endoscopic probes such as nasopharyngeal and gastrointestinal cancers. Studies in progress in our laboratory are investigating the potential of detecting similar effects with lower frequency ultrasound down to 5 MHz that might enlarge the range of applications.

### CONCLUSION

Ultrasound imaging (10–30 MHz) and quantitative ultrasonic methods were used to detect responses to radiotherapy *in vitro* and differentiate between cells that die predominantly by mitotic arrest/catastrophe from cells that die predominantly by a mix of apoptosis and mitotic arrest. Experimental evidence supports the basis for ultrasonic detection of radiotherapy effects to be changes in size and potentially size variance of cells and nuclei after apoptosis, mitotic arrest, and mitotic catastrophe. The technique can be applied preclinically *in vivo* on tumors grown subcutaneously in mice for ultrasonic characterization of tumor responses to radiotherapy (26). The results indicate that these cell structural changes have a strong influence on ultrasound backscatter and SS, providing a framework for future experiments with the goal of demonstrating the potential of rapidly and noninvasively monitoring and differentiating the effects of radiotherapy and other anticancer treatments using an ultrasound-based approach.

### REFERENCES

- Weber WA, Figlin R. Monitoring cancer treatment with PET/CT: Does it make a difference? *J Nucl Med* 2007;48:36S–44S.
- Erasmus JJ, Munden RF. The role of integrated computed tomography positron-emission tomography in esophageal cancer: Staging and assessment of therapeutic response. *Semin Radiat Oncol* 2007;17:29–37.
- Brasch RC, Li KC, Husband JE, et al. *In vivo* monitoring of tumor angiogenesis with MR imaging. *Acad Radiol* 2000;7:812–823.
- Preda A, Wielopolski PA, Ten Hagen TL, et al. Dynamic contrast-enhanced MRI using macromolecular contrast media for monitoring the response to isolated limb perfusion in experimental soft-tissue sarcomas. *MAGMA* 2004;17:296–302.
- Lassau N, Lamuraglia M, Vanel D, et al. Doppler US with perfusion software and contrast medium injection in the early evaluation of isolated limb perfusion of limb sarcomas: Prospective study of 49 cases. *Ann Oncol* 2005;16:1054–1060.
- Lizzi FL, Feleppa EJ, Kaiser AS, et al. Ultrasonic spectrum analysis for tissue evaluation. *Pattern Recognition Letters* 2003;24:637–658.
- Lizzi FL, King DL, Rorke MC, et al. Comparison of theoretical scattering results and ultrasonic data from clinical liver examinations. *Ultrasound Med Biol* 1988;14:377–385.
- Yang M, Krueger TM, Miller JG, et al. Characterization of anisotropic myocardial backscatter using spectral slope, intercept and midband fit parameters. *Ultrason Imaging* 2007;29:122–134.
- Oelze ML, O'Brien WD Jr., Blue JP, et al. Differentiation and characterization of rat mammary fibroadenomas and 4T1 mouse carcinomas using quantitative ultrasound imaging. *IEEE Trans Med Imaging* 2004;23:764–771.
- Feleppa EJ, Kalisz A, Melgar S, et al. Typing of prostate tissue by ultrasonic spectrum analysis. *IEEE Trans Ultrason Ferroelectr Freq Control* 1996;43:609–619.
- Balaji KC, Fair WR, Feleppa EJ, et al. Role of advanced 2 and 3-dimensional ultrasound for detecting prostate cancer. *J Urol* 2002;168:2422–2425.
- Tannock IF, Hill RP, Bristow RG, et al. *The basic science of oncology*. 4th ed. New York: McGraw-Hill; 2005.
- Czarnota GJ, Kolios MC, Abraham J, et al. Ultrasound imaging of apoptosis: High-resolution non-invasive monitoring of programmed cell death *in vitro*, *in situ* and *in vivo*. *Br J Cancer* 1999;81:520–527.
- Kolios MC, Czarnota GJ, Lee M, et al. Ultrasonic spectral parameter characterization of apoptosis. *Ultrasound Med Biol* 2002;28:589–597.
- Kolios MC, Czarnota GJ. New insights into high frequency ultrasonic tissue scattering [Abstract]. In the 11th International Symposium on Advanced Biomedical Ultrasound, Sendai, Japan 2008.
- Wang C, Koistinen P, Yang GS, et al. Mast cell growth factor, a ligand for the receptor encoded by c-kit, affects the growth in culture of the blast cells of acute myeloblastic leukemia. *Leukemia* 1991;5:493–499.
- Taggart LR, Baddour RE, Giles A, et al. Ultrasonic characterization of whole cells and isolated nuclei. *Ultrasound Med Biol* 2007;33:389–401.
- Lizzi FL, Astor M, Feleppa EJ, et al. Statistical framework for ultrasonic spectral parameter imaging. *Ultrasound Med Biol* 1997;23:1371–1382.
- Lizzi FL, Greenebaum M, Feleppa EJ, et al. Theoretical framework for spectrum analysis in ultrasonic tissue characterization. *J Acoust Soc Am* 1983;73:1366–1373.
- Crocker MJ. *Encyclopedia of acoustics*. New York: Wiley; 1997.
- Pozarowski P, Grabarek J, Darzynkiewicz Z. Flow cytometry of apoptosis. *Curr Protoc Cell Biol* 2004; Chapter 18:Unit 18.8.
- Lizzi FL, Ostromogilsky M, Feleppa EJ, et al. Relationship of ultrasonic spectral parameters to features of tissue microstructure. *IEEE Trans Ultrason Ferroelectr Freq Control* 1987;34:319–329.
- Darzynkiewicz Z, Juan G, Li X, et al. Cytometry in cell necrobiology: Analysis of apoptosis and accidental cell death (necrosis). *Cytometry* 1997;27:1–20.
- Hunt JW, Worthington AE, Kerr AT. The subtleties of ultrasound images of an ensemble of cells: Simulation from regular and more random distributions of scatterers. *Ultrasound Med Biol* 1995;21:329–341.
- Hunt JW, Worthington AE, Xuan A, et al. A model based upon pseudo regular spacing of cells combined with the randomisation of the nuclei can explain the significant changes in

- high-frequency ultrasound signals during apoptosis. *Ultrasound Med Biol* 2002;28:217–226.
26. Vlad RM, Brand S, Giles A, *et al.* Quantitative ultrasound assessing tumor responses to radiotherapy in cancer mouse models [Abstract]. *Ultrasonic Imaging* 2008;29:255–256.
  27. Vlad RM, Czarnota GJ, Giles A, *et al.* High-frequency ultrasound for monitoring changes in liver tissue during preservation. *Phys Med Biol* 2005;50:197–213.
  28. Vlad RM, Orlova V, Hunt JW, *et al.* Changes measured in the backscatter ultrasound signals during cell death can be potentially explained by an increase in cell size variance [Abstract]. *Ultrasonic Imaging* 2008;29:256.
  29. Ursea R, Coleman DJ, Silverman RH, *et al.* Correlation of high-frequency ultrasound backscatter with tumor microstructure in iris melanoma. *Ophthalmology* 1998;105:906–912.
  30. Lizzi FL. Ultrasonic scatterer-property images of the eye and prostate. *IEEE Ultrasonics Symposium Proceedings* 1997;2:1109–1118.
  31. Lightdale CJ, Kulkarni KG. Role of endoscopic ultrasonography in the staging and follow-up of esophageal cancer. *J Clin Oncol* 2005;23:4483–4489.